AIAA JOURNAL
Vol. 49, No. 7, July 2011

Study of Biologically Inspired Flapping Mechanism for Micro Air Vehicles

Zaeem A. Khan*
GE Global Research, Niskayuna, New York 12309
and
Sunil K. Agrawal†
University of Delaware, Newark, Delaware 19716

DOI: 10.2514/1.J050447

This paper explores the design of a flapping mechanism inspired by the insect thorax. A two-degree-of-freedom model of the insect thorax is developed that governs the flapping and rotational (pitching) motions of the wing. The wing kinematics are optimized experimentally using a dynamically scaled wing driven by a robotic flapper. Next, optimal parameters of the thorax model are determined in order to generate the optimal wing kinematics. For this purpose, analytical methods as well as numerical optimization are used. This analysis also reveals the significance of the mechanical design of the insect wing in improving aerodynamic performance. A prototype mechanism is developed based on the thorax model. Experimental evaluation of the mechanism shows good agreement with theoretical results. Additionally, the design is very simple and shows substantial lift generation capability.

Nomenclature

C_a	=	aerodynamic damping coefficient, kg · m^2
C_L	=	cycle-averaged coefficient of lift for entire wing
$\bar{D}$	=	cycle-averaged aerodynamic drag, gf
f	=	flapping frequency; $\omega_e/2\pi$, Hz
J	=	moment of inertia about flap axis ($\hat{z}_s$ axis), kg · m^2
J_x	=	moment of inertia of wing about the $\hat{x}_w$ axis in wing frame $\mathcal{F}_w$, kg · m^2
J_y	=	moment of inertia of wing about wing leading edge or $\hat{y}_w$ axis, kg · m^2
J_{yz}	=	product of inertia of wing, kg · m^2
K_{f1}, K_{f2}	=	parameters of nonlinear flapping spring, N · m/rad and N · m/rad^3, respectively
K_{r1}, K_{r2}	=	parameters of nonlinear rotational spring, N · m/rad and N · m/rad^3, respectively
$\bar{L}$	=	cycle-averaged aerodynamic lift
r_i	=	distance between wing base **B** and ith blade element
T	=	wing beat period; $1/f$, s
t	=	time, s
α^*	=	constant geometric angle of attack during flapping phase; $\pi/2 - \theta_r^*$, °
ΔT	=	time during which the wing rotates at the end of each stroke, s
Θ_e	=	excitation amplitude, °
Θ_f	=	amplitude of flapping motion or stroke amplitude, °
θ_e	=	wing excitation angle, °
θ_f	=	flap angle, °
θ_r	=	wing rotation angle, °
Θ_f^*	=	peak stroke amplitude, °
θ_r^*	=	amplitude of rotation, °
μ_r	=	viscous damping coefficient for rotational motion, N · m/s
τ	=	nondimensional time, $t \cdot \sqrt{K_{f1}/J_x}$
ϕ_r	=	phase between flapping and rotational motions, °
ω_e	=	excitation frequency or flapping frequency, rad/s
ω_e^*	=	excitation frequency at peak stroke amplitude Θ_f^*, rad/s

Received 20 January 2010; revision received 28 July 2010; accepted for publication 13 December 2010.

*Mechatronics Engineer; zaeem.khan@ge.com.
†Professor and Director Mechanical Systems Laboratory, Department of Mechanical Engineering; agrawal@udel.edu.

I. Introduction

MICRO air vehicles (MAVs) are an emerging class of aerial vehicles that can be used for numerous applications due to their small size. These include search and rescue operations in confined places, remote sensing of hazardous leaks, inspection of hard-to-reach places in industrial plants, and surveillance in crime and hostage situations. Natural MAVs, such as insects and hummingbirds, satisfy all the key design requirements to fulfill these missions. Hence, there is a need to develop biomimetic flapping-wing MAVs or FWMAVs.

In the quest for developing FWMAVs, engineers have focused on the design of flapping mechanisms for generating insectlike wing motion. Primarily, two different approaches were taken: rigid-link mechanisms and resonant mechanisms. The total power required for flapping-wing flight is composed of aerodynamic power to generate lift and inertial power. The inertial power is due to the excess wing kinetic energy that, if not stored, shows up as impact loads at the end of each stroke. Insects store wing kinetic energy as strain energy in the highly elastic thorax exoskeleton [1–3]. Because of lack of energy storage, rigid-link mechanisms waste kinetic energy in impact loads. This requires additional structural strength, which makes the design heavier for flight [4,5]. Therefore, resonant mechanisms are more efficient for FWMAVs [6,7].

Insect wing motion primarily consists of flapping, rotation (pitching), and deviation motions (Fig. 1). Flapping is the beating of wings in a plane called the stroke plane, denoted by angle θ_f. During flapping, a nearly constant angle of attack α^* is maintained. Near the end of each stroke, the wing rotates or flips (denoted by θ_r) about the leading edge in order to set α^* for the subsequent stroke. Finally, angle θ_d describes the deviation of the wing out of the stroke plane.

Typically, in the design of flapping mechanisms, the aim has been to minimize the error between the wingtip trajectory generated by the mechanism and a given insect wingtip trajectory [4–6]. However, this ignores wing rotation, which has a significant lift contribution if the phase between flapping and rotational motions is optimized [8]. On the other hand, deviational motion was found to have minimal effect [9]. Another problem with this approach is that mimicking a particular insect wing motion does not guarantee peak aerodynamic

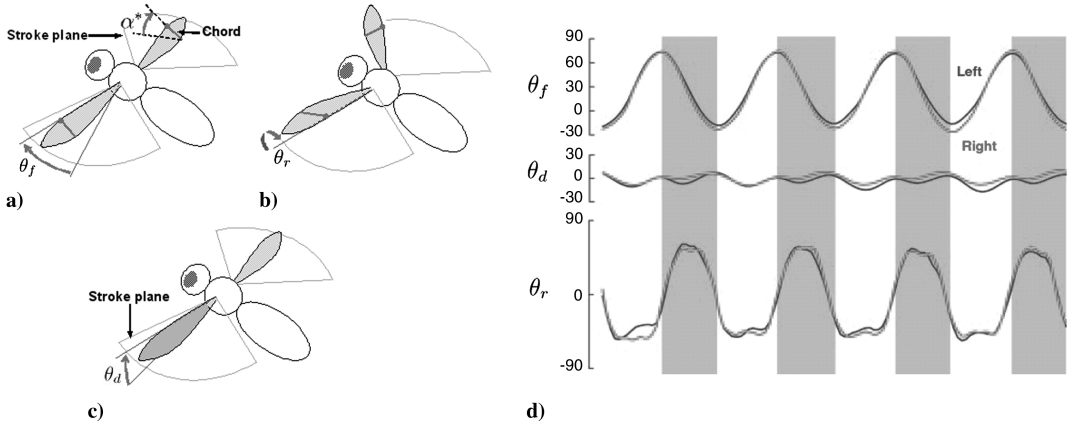

Fig. 1 Schematic showing insect wing motion: a) flapping, b) rotation, c) deviation, and d) (modified from [10]) time trajectories of left and right wing motions of honeybee during hovering flight.

performance [10]. Therefore, this approach disconnects wing kinematics and optimal aerodynamic performance. In contrast, the University of California, Berkeley, micromechanical flying insect (MFI) design team developed a microscale resonant mechanism that generates flapping and rotational motions by means of two actuators [11]. This allows MFI design to maintain the optimal phase between flapping and rotational motions [12]. Recently, Wood [13] demonstrated successful tethered liftoff of a robotic insect actuated by a mechanism similar to MFI but using a single actuator and passive wing rotation.

In our previous work [14], we used a robotic flapping-wing device to determine the optimal wing kinematics for maximizing the cycle-averaged lift and the lift-to-drag ratio. The results showed that maximizing stroke amplitude and optimizing the phase between flapping and rotational motion improves aerodynamic performance. In addition, we developed a dynamical model of *Diptera* thorax. The thorax model was tuned to operate at resonance (peak stroke amplitude) by using numerical simulations to generate the frequency response. The parameters of the flapping dynamics equation were tweaked to achieve the desired resonant frequency. This was a trial and error approach [14,15]. In this paper, we take this work one step further by deriving an algebraic relationship between the peak stroke amplitude and parameters of the flapping dynamics equation using perturbation analysis. This analysis further reveals that flapping dynamics are stable when excited at resonance. The optimal rotational motion is further analyzed to understand the cause of increased aerodynamic performance due to phase optimization.

The outline of the paper is as follows. Section II describes the aeromechanical model of insect-thorax actuation. Section III summarizes the experiments used to determine the optimal wing kinematics. In Sec. IV, nondimensionalization is used to show that the flapping dynamics can be decoupled from the rotational dynamics, and thus a simplified thorax model is derived. Section V presents the perturbation analysis, which results in an algebraic relationship between the peak stroke amplitude and the parameters of the flapping dynamics equation. The optimization of rotational dynamics is presented in Sec. VI. Section VII presents the design, implementation, and testing of a flapping mechanism prototype based on the thorax model. This prototype is also used as a testbed to validate the theoretical findings. Finally, Sec. VIII presents a summary and conclusions.

II. Model of Insect Thorax

The insect thorax consists of a highly elastic exoskeleton containing flight muscles. These muscles deform the exoskeleton so that the tergal plate moves up and down, causing the wings to flap through a hinge mechanism, as shown in Figs. 2a and 2b. The excess kinetic energy of the wing is stored as strain energy due to deformation of the thorax exoskeleton, shown shaded in Figs. 2a and 2b. Note that θ_e is the excitation angle, which represents flapping motion assuming no deformation of exoskeleton. The difference $\theta_f - \theta_e$ indicates deformation or storage of strain energy. As the wing flaps, it twists passively along the span at the end of each stroke due to the aerodynamic and inertial loads, as shown in Fig. 2c. In small insects, such as honeybees and flies, the twist occurs very close to the wing base. The rest of the wing rotates almost like a rigid plate by an angle θ_r [8,10]. The remarkable design of insect wing structure prevents rotation beyond $\theta_r = \theta_r^*$ to maintain angle of attack $\alpha^* = \pi/2 - \theta_r^*$ due to a sharp increase of rotational stiffness [16]. This can also be

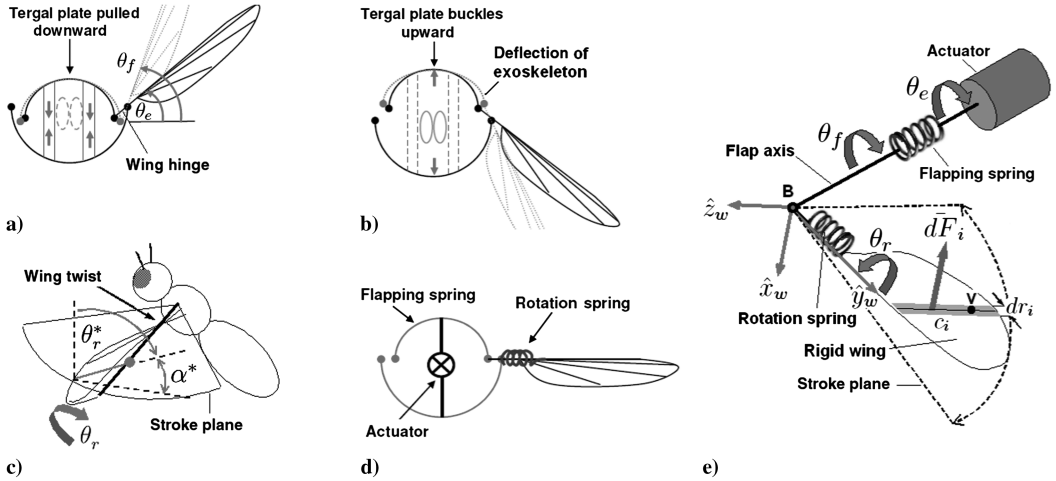

Fig. 2 Schematic showing the working of insect thorax: a and b) generation of flapping motion, c) rotational motion, and d and e) simplified model to capture essential mechanics of insect thorax.

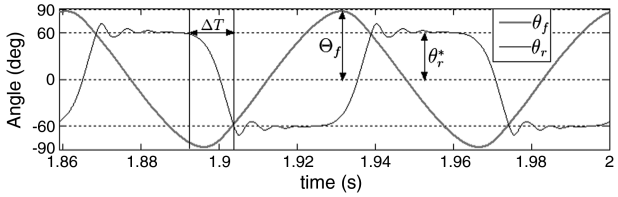

Fig. 3 Numerical simulation of Eq. (1) after reaching steady state. $\Theta_f \approx 90°$ and $\theta_r^* = 60°$ or $\alpha^* = 30°$.

observed in Fig. 1d, where θ_r trajectories are nearly constant or flat between rotations.

We model the thorax flapping mechanism by replacing the flight muscles by an actuator; the tergal plate and the elastic wing twist are modeled by nonlinear flapping and rotational springs, respectively (Fig. 2d). The wing is assumed to be rigid, which undergoes flapping and rotational motion. A coordinate frame $\mathcal{F}_w$: $(\hat{x}_w, \hat{y}_w, \hat{z}_w)$ is attached to the wing, with the origin located at the wing base **B** (Fig. 2e). The $\hat{x}_w$ axis is normal to the wing surface, the $\hat{y}_w$ axis (rotation axis) is in the spanwise direction along the wing leading edge, and $\hat{z}_w$ is along the chordwise direction.

A. Equations of Motion

The equations of motion are derived using the Lagrangian method. Detailed derivation is presented elsewhere [14]. Here, we only present the equations in their final form as follows:

$$M(q)\ddot{q} + C(q,\dot{q}) + G(q) = Q(q,\dot{q}) \tag{1}$$

where $q = (\theta_f, \theta_r)^T$ and

$$M(q) = \begin{pmatrix} \sin^2\theta_r J_x + \cos^2\theta_r J_z & \cos\theta_r J_{yz} \\ \cos\theta_r J_{yz} & J_y \end{pmatrix}$$

$$C(q,\dot{q}) = \begin{pmatrix} (J_x - J_z)\sin(2\theta_r)\dot{\theta}_f\dot{\theta}_r - J_{yz}\sin\theta_r\dot{\theta}_r^2 \\ -\frac{1}{2}(J_x - J_z)\sin(2\theta_r)\dot{\theta}_f^2 \end{pmatrix}$$

$$G(q) = \begin{pmatrix} -K_{f1}(\theta_e - \theta_f) - K_{f2}(\theta_e - \theta_f)^3 \\ K_{r1}\theta_r + K_{r2}\theta_r^3 + K_{r3}\theta_r \end{pmatrix}$$

$$Q(q,\dot{q}) = \begin{pmatrix} -\cos\theta_r \sum_{i=1}^{N} r_i dF_i \\ -C_2 \sum_{i=1}^{N} c_i dF_i - \mu_r\dot{\theta}_r \end{pmatrix}$$

where J_x, J_z and J_{yz} are the wing moments and product of inertia in $\mathcal{F}_w$ frame, $\theta_e = \Theta_e \cos\omega_e t$ is the sinusoidal excitation angle where Θ_e is the excitation amplitude, and ω_e is the excitation frequency. K_{f1}, K_{f2} are the parameters of the flapping spring and K_{r1}, K_{r2}, K_{r3} are parameters of the rotation spring. The parameter K_{r3} models the sharp increase in rotational stiffness, which locks the wing at α^*. Note that $K_{r3} = 0$ if $|\theta_r| < \theta_r^*$ and it is nonzero if $|\theta_r| \geq \theta_r^*$, where θ_r^* equals $\pi/2 - \alpha^*$. For the lock to take effect, $K_{r3} \gg K_{r1}, K_{r2}$.

B. Aerodynamic Model

The $Q(q,\dot{q})$ vector contains the aerodynamic model of flapping wings based on the blade element method in which the wing is divided into N elements. As shown in Fig. 2e, for an ith element having a cord c_i and width dr_i, the differential aerodynamic force vector is given by

$$\overline{dF}_i = dF_i\hat{x}_w = (C_1(\alpha_i)\tfrac{\rho}{2}|\bar{V}_i|^2 c_i dr_i)\hat{x}_w \tag{2}$$

where $\overline{dF}_i$ is assumed to act normal to the wing due to the dominance of pressure force [17], $C_1(\alpha_i)$ is a coefficient of normal force, which is a function of the angle of attack α_i of the ith element, $\bar{V}_i$ is the flow velocity vector, and ρ is the density of air. Based on a model by Walker [18], the rotational force peaks are modeled by computing $\bar{V}_i$ at a point v along the chord at each blade element (see Fig. 2e). Point v is located at a distance of $C_2 c_i$ from the leading edge, where C_2 is a coefficient of rotational force and is embedded in the expression for $\bar{V}_i$. Both C_1 and C_2 can be determined by experiments. Further details about the aerodynamic model can be found in [14,19].

C. Computer Simulation

The equations of motion, along with the aerodynamic model, constitute the complete model of the system. The numerical simulation of this system after reaching steady state is shown in Fig. 3. The motion is qualitatively similar to the insect wing motion (see Fig. 1d). The flapping motion is nearly sinusoidal, while the rotational motion is trapezoidal and marked by overshoots after the wing flips. Note that θ_r varies very little from θ_r^* due to the presence of the K_{r3} term. These insectlike kinematics can be described by a few parameters, which allow variations in kinematics without changing them qualitatively. These are the stroke amplitude Θ_f, the constant angle of attack $\alpha^* = \pi/2 - \theta_r^*$, the phase ϕ_r between the flapping and rotational motion, and the duration of rotation ΔT, which is a measure of how fast the wing rotates [9].

III. Optimal Hovering Kinematics

We now determine the optimal set of kinematic parameters $\{\Theta_f, \alpha^*, \phi_r, \Delta T\}$ for maximum aerodynamic performance. To describe aerodynamic performance, we define lift $\bar{L}$, drag $\bar{D}$, and coefficient of lift C_L averaged over the wing beat cycle as follows:

$$\bar{L} = \frac{1}{T}\int_o^T L(t)\,\mathrm{d}t, \qquad \bar{D} = \frac{1}{T}\int_o^T |D(t)|\,\mathrm{d}t$$

$$C_L = \frac{\bar{L}}{0.5\rho S_2(\pi f \Theta_f)^2} \tag{3}$$

where $L(t)$ and $D(t)$ are time-varying lift and drag forces, ρ is the density of air, and

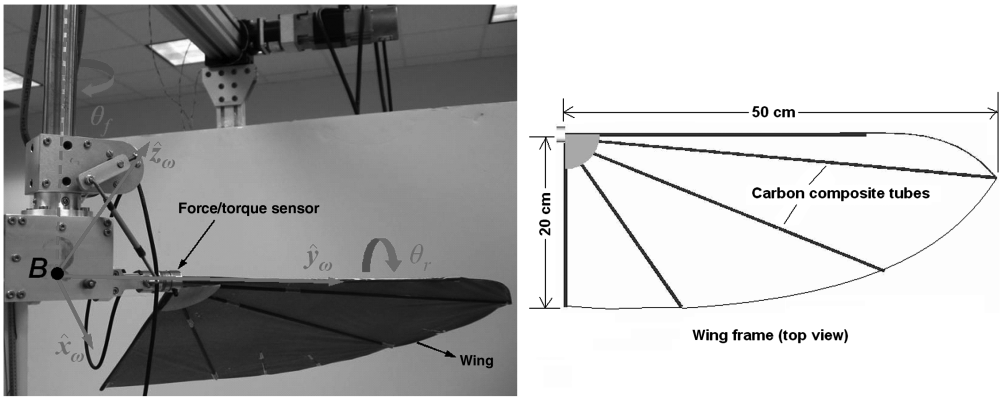

Fig. 4 Robotic flapper designed and fabricated at University of Delaware and wing planform geometry used for testing.

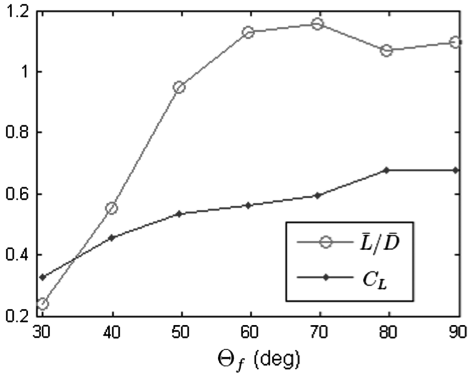

Fig. 5 Effect of varying Θ_f on C_L and $\bar{L}/\bar{D}$ ratio at $Re = 18,326$.

$$S_2 = 2\sum_{i}^{N} c_i dr_i$$

is the second moment of wing area [1]. The criteria for aerodynamic performance is high C_L at a high $\bar{L}/\bar{D}$ ratio. To characterize the optimal kinematics, a robotic flapping-wing device is used, which can provide (θ_f, θ_r) motion via two independent servomotors (see Fig. 4). At the base of the wing, a sensor detects the aerodynamic force and torque as the wing moves. The sensor data are filtered online using a first-order filter, and they are filtered offline with a zero-phase delay, low-pass Butterworth filter with a cutoff frequency set to 15 times the flapping frequency.

To obtain dynamic scaling, the Reynolds number Re for flapping wings [20] is matched between the flapper wing and a one-fifth-scale FWMAV wing. Since the thorax model assumes a rigid, untwisted wing, the scaled-up wing is fabricated with carbon tubes and covered with mylar. This ensures rigidity; however, the mylar membrane billows slightly due to aerodynamic loads. The gravity and inertial loads are computed online using Newton–Euler equations of the rigid wing and subtracted from the sensor output to obtain the pure aerodynamic loads in the wing frame $\mathcal{F}_w$ (see Fig. 4). From $\mathcal{F}_w$, the data are transformed into the lift and drag axes, which are normal and parallel, respectively, to the stroke plane. To determine optimal kinematic parameters, we start with nominal values ($\Theta_f = 30°$, $\alpha^* = 35°$, $\phi_r \equiv 0°$, $\Delta T \equiv$ nominal) and vary each parameter in a sequence of experiments as follows.

A. Optimal Stroke Amplitude Θ_f

In the first experiment, Θ_f is varied from 30 to 90°, in 10° increments, while keeping the product $f\Theta_f$ constant. This ensures constant values of Re and the denominator of C_L for all values of Θ_f. The experimental results presented in Fig. 5 clearly show an increase of $\bar{L}/\bar{D}$ and C_L with Θ_f. However, by manipulating rotational motion, aerodynamic performance could be improved even further. This leads us to the second experiment.

B. Optimal Rotational Motion

In the second experiment, Θ_f is fixed at 90°, while ΔT is varied from nominal to fast and slow, as shown in Fig. 6a, and for each ΔT, the phase ϕ_r is varied from −30° (delayed flip) to 30° (advanced flip) in 5° increments, as shown in Fig. 6b.

The experimental results presented in Figs. 6c and 6d show that advanced flip ($\phi_r > 0°$) results in an increase of C_L as well as $\bar{L}/\bar{D}$. Maximum $\bar{L}/\bar{D}$ occurs at values of ϕ_r between 5 and 15°, while C_L increases almost linearly with ϕ_r. Furthermore, ΔT has very little effect on C_L; however, the nominal and fast wing rotation increases $\bar{L}/\bar{D}$ compared with the slow flip case. Therefore, by manipulating the rotational motion, we are able to significantly improve $\bar{L}/\bar{D}$ and C_L at $\Theta_f = 90°$ compared with the data in Fig. 5.

This experiment was repeated at $\Theta_f = 40°$ to see the effects at smaller stroke amplitudes. The results showed similar variation of C_L and $\bar{L}/\bar{D}$ but significantly lower magnitudes compared with $\Theta_f = 90°$ case. This again confirms the importance of large Θ_f.

C. Optimal Angle of Attack α^*

In the preceding experiments, α^* was maintained at 35°. In this experiment, we fix $\Theta_f = 90°$ and $\Delta T =$ nominal, while α^* is varied from 10 to 70°, in 5° increments. The experiment is repeated for five values of $\phi_r(-5, 0, 5, 10, 15°)$, which include the optimal range of ϕ_r found in the previous experiment.

The results given in Fig. 7 show that maximum $\bar{L}/\bar{D}$ occurs at $\alpha^* = 15°$, but maximum C_L occurs at $\alpha^* = 55°$. Therefore, optimal α^* is a compromise between maximum C_L and $\bar{L}/\bar{D}$. A good compromise can be achieved in the range $25° < \alpha^* < 40°$, which is used by most insects and hummingbirds [1,21]. The results again show that $\phi_r < 0°$ decreases $\bar{L}/\bar{D}$ and C_L (see the curve of $\phi = -5°$ in Fig. 7).

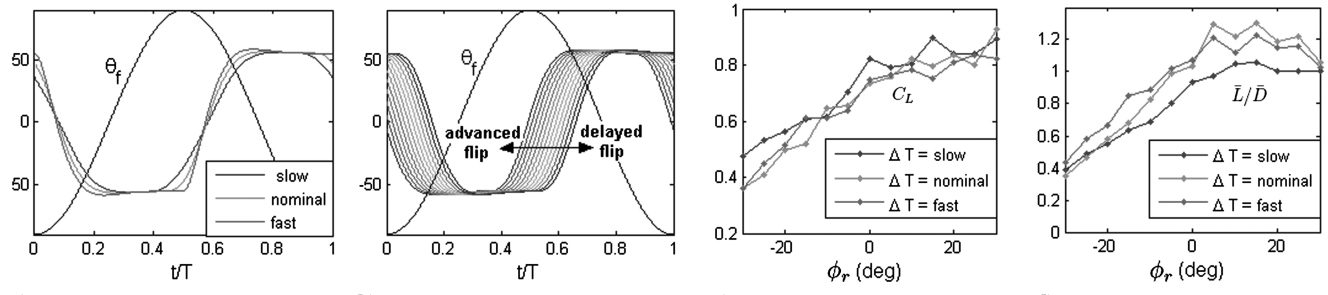

a) b) c) d)

Fig. 6 Effect of variation of ΔT and phase ϕ_r on C_L and $\bar{L}/\bar{D}$ ratio at $Re = 18,326$.

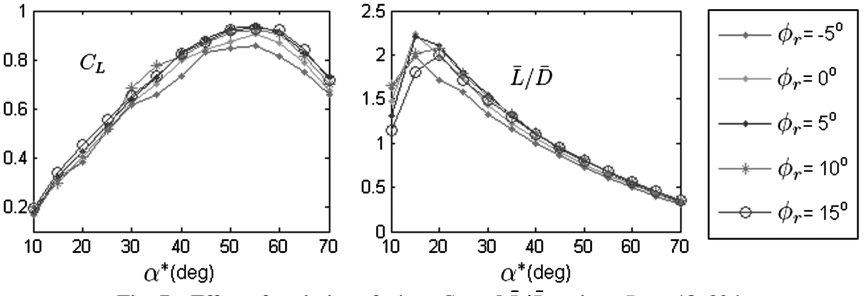

Fig. 7 Effect of variation of α^* on C_L and $\bar{L}/\bar{D}$ ratio at $Re = 18,326$.

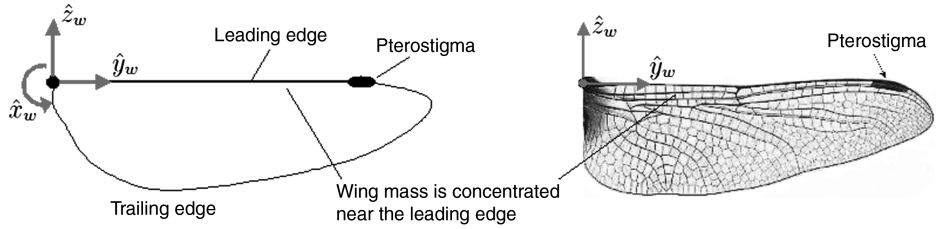

a) b)

Fig. 8 Wing mass mainly concentrated near leading edge or rotation axis. Veins become thin toward the trailing edge. Also shown is location of pterostigma on dragonfly wing.

IV. Simplified Thorax Model

In this section, the parameters of the thorax model are determined in order to generate optimal kinematics. For this purpose, a simplified thorax model is derived as follows.

The pattern of venation distribution in insect wings shifts the center of mass near the leading edge or $\hat{y}_w$ axis [2] (Fig. 8). This means $J_x \approx J_z = J$ and J_{yz}, $J_y \ll J$. The implication of this can be seen if we nondimensionalize Eq. (1) by dividing with J and scaling time by using $\tau = \omega_o t$, where $\omega_o = \sqrt{K_{f1}/J}$. Notice that the coefficient of $\ddot{\theta}_f$ in $M(q)$ becomes one, while other terms are much smaller than one. Similarly, the coefficients of terms in the $C(q, \dot{q})$ vector become negligible compared with one. Therefore, flapping dynamics are decoupled from rotational dynamics, except for coupling in $Q(q, \dot{q})$ due to the aerodynamic model.

If we assume that the wing maintains optimal α^* during the flapping phase and flips instantaneously without actually rotating (i.e., $\Delta T = 0$), then the aerodynamic model is greatly simplified and flapping dynamics are decoupled. The simplified thorax dynamics model with the decoupled flapping dynamics equation is given by

$$J\ddot{\theta}_f = K_{f1}(\Theta_e \cos\omega_e t - \theta_f) + K_{f2}(\Theta_e \cos\omega_e t - \theta_f)^3 - C_a\dot{\theta}_f|\dot{\theta}_f| \tag{4}$$

$$J_y\ddot{\theta}_r = \frac{(J_x - J_z)}{2}\dot{\theta}_f^2 \sin 2\theta_r - J_{yz}\ddot{\theta}_f \cos\theta_r - K_{r1}\theta_r - K_{r2}\theta_r^3 - K_{r3}\theta_r - C_2\sum_{i=1}^{N} c_i dF_i - \mu_r\dot{\theta}_r \tag{5}$$

where J is the wing inertia about the flap axis (see Fig. 2e), $C_a\dot{\theta}_f|\dot{\theta}_f|$ is the aerodynamic torque about the flapping axis, which is independent of $\dot{\theta}_r$. Here, C_a is the aerodynamic damping coefficient, which is a function of wing geometry and α^*. It is given by

$$C_a = C_1(\alpha^*)\frac{\rho}{2}\cos(\pi/2 - \alpha^*)\sum_{i=1}^{N} r_i^3 c_i dr_i \tag{6}$$

The decoupled flapping dynamics equation can be studied independently. However, the rotational dynamics are highly dependent on flapping dynamics, as can be seen from the first two terms on the right side of Eq. (6) involving $\dot{\theta}_f$ and $\ddot{\theta}_f$. Therefore, we first optimize flapping dynamics and then the rotational dynamics in the following sections.

V. Optimal Flapping Dynamics

The key aerodynamic requirement with regard to flapping motion is large Θ_f. Since the flapping dynamics equation represents a mechanical oscillator, the peak stroke amplitude Θ_f^* occurs at the resonant frequency ω_e^*. In this section, Θ_f^* and ω_e^* are determined analytically as a function of parameters in the flapping dynamics equation. In nondimensional form, the flapping dynamics equation is given by

$$\ddot{\theta}_f + \theta_f = \Theta_e \cos\Lambda\tau + \frac{K_{f2}}{K_{f1}}(\Theta_e \cos\Lambda\tau - \theta_f)^3 - \frac{C_a}{J}\dot{\theta}_f|\dot{\theta}_f| \tag{7}$$

where C_a/J is the nondimensional aerodynamic damping coefficient, $\Lambda = \omega_e/\omega_o$ is the nondimensional driving frequency, and K_{f2}/K_{f1} characterizes the nonlinearity of the flapping spring.

Table 1 shows the values of C_a/J computed for some insects and hummingbirds in order of increasing body mass and wing length [1,21]. Note that $C_a/J \ll 1$ for all species, irrespective of size and mass. The excitation amplitude Θ_e is proportional to the movement of the tergal plate and is a function of wing hinge geometry. However, this relationship is not known for any insect. Since the movement of the tergal plate is very small, we assume that $\Theta_e \ll 1$. In addition, if we consider weak nonlinearity in stiffness (i.e., $K_{f2}/K_{f1} \ll 1$, then the following change of variables can be made:

$$\epsilon B = \frac{C_a}{J}, \qquad \epsilon K = \frac{K_{f2}}{K_{f1}}, \qquad \epsilon F = \Theta_e \tag{8}$$

where B, K, and F are $O(1)$ and $\epsilon \ll 1$. Substituting these in Eq. (7), we get

$$\ddot{\theta}_f + \theta_f = \epsilon h(\theta_f, \dot{\theta}_f, \tau) = \epsilon[F\cos\Lambda\tau + K(\epsilon F\cos\Lambda\tau - \theta_f)^3 - B\dot{\theta}_f|\dot{\theta}_f|] \tag{9}$$

This equation is in the form of a weak nonlinear oscillator, which is a perturbation of the linear oscillator $\ddot{\theta}_f + \theta_f = 0$ when $\epsilon = 0$. All the nonlinearities are included in the function $h(\theta_f, \dot{\theta}_f, \tau)$ on the right-hand side. Analytical solutions of equations of this form can be derived using perturbation techniques, such as the method of averaging [22–24]. In this method, we make the following change of variables:

$$\theta_f(\tau) = \Theta_f(\tau)\cos[\tau + \zeta(\tau)], \qquad \dot{\theta}_f(\tau) = -\Theta_f(\tau)\sin[\tau + \zeta(\tau)] \tag{10}$$

Table 1 C_a/J for some insects and hummingbirds

	Species	Body mass, g	Wing length, mm	C_a/J
1	Ladybug beetle (*Coccinella*)	0.0359	11.7	0.0118
2	Dragonfly (*Aeschna juncea*)	0.754	47.4	0.0389
3	Hawk moth (*Manduca sexta*)	1.32	51.8	0.0122
4	Hummingbird (*Amazilia fimbriata*)	5.1	58.5	0.005
5	Hummingbird (*Lampornis clemenciae*)	8.4	85.0	0.0077

where Θ_f and ζ are slowly time varying for $0 < \epsilon \ll 1$. This transforms Eq. (9) into two first-order equations governing the amplitude Θ_f and phase ζ of the oscillator, given by

$$\dot{\Theta}_f = -\epsilon h(\Theta_f c_\xi, -\Theta_f s_\xi, \tau) s_\xi$$
$$\dot{\zeta}\Theta_f = -\epsilon h(\Theta_f c_\xi, -\Theta_f s_\xi, \tau) c_\xi \tag{11}$$

where $c_\xi = \cos\xi$, $s_\xi = \sin\xi$, and $\xi = \tau + \zeta$. This system has two time scales: a fast time scale of sinusoidal oscillations of period 2π, with respect to the variable ξ, and a slow time scale due to ϵ on the right side of Eqs. (11). Since the system varies little over the fast time scale, it can be averaged over this period to obtain the following time-averaged system:

$$\dot{\Theta}_f = -\frac{\epsilon}{2\pi}\int_o^{2\pi} h(\Theta_f c_\xi, -\Theta_f s_\xi, \tau) s_\xi \, \mathrm{d}\xi$$
$$\dot{\zeta}\Theta_f = -\frac{\epsilon}{2\pi}\int_o^{2\pi} h(\Theta_f c_\xi, -\Theta_f s_\xi, \tau) c_\xi \, \mathrm{d}\xi \tag{12}$$

Since the oscillator is analyzed near resonance, we assume Λ is close to one. This can be written as $\Lambda = 1 + \epsilon\sigma$, where σ is $O(1)$ and $\epsilon \ll 1$. Substituting this and integrating Eqs. (12), keeping only slowly varying terms, gives the following averaged, nonautonomous system:

$$\dot{\Theta}_f = \epsilon\left[\frac{F}{2}\sin(\epsilon\sigma\tau - \zeta) - \frac{4B}{3\pi}\Theta_f^2\right]$$
$$\dot{\zeta}\Theta_f = \epsilon\left[-\frac{F}{2}\cos(\epsilon\sigma\tau - \zeta) + \frac{3k}{8}\Theta_f^3\right] \tag{13}$$

A change of variable $\gamma = \epsilon\sigma\tau - \zeta$ and converts it into an autonomous system:

$$\dot{\Theta}_f = \epsilon\left(\frac{F}{2}\sin\gamma - \frac{4B}{3\pi}\Theta_f^2\right)$$
$$\dot{\gamma}\Theta_f = \epsilon\left(\frac{F}{2}\cos\gamma + \sigma\Theta_f - \frac{3k}{8}\Theta_f^3\right) \tag{14}$$

At steady state, $\dot{\Theta}_f = \dot{\gamma} = 0$, which results in the following algebraic relationship:

$$\frac{F}{2}\sin\gamma = \frac{4B}{3\pi}\Theta_f^2, \qquad \frac{F}{2}\cos\gamma = -\left(\Theta_f\sigma - \frac{3k}{8}\Theta_f^3\right) \tag{15}$$

The equilibrium states (Θ_f, γ) are solution of Eqs. (15). Eliminating γ from Eq. (15) gives

$$\frac{16B^2}{9\pi^2}\Theta_f^4 + \left(\Theta_f\sigma - \frac{3k}{8}\Theta_f^3\right)^2 = \frac{F^2}{4} \tag{16}$$

This is a cubic equation in Θ_f^2 involving the parameters F and B and the nondimensional driving frequency σ. Since peak stroke amplitude is required, we apply $\mathrm{d}\Theta_f/\mathrm{d}\sigma = 0$ in Eq. (16), which gives $\sigma = \frac{3k}{8}\Theta_f^2$. Substituting this result in Eq. (15) results in $\frac{F}{2}\cos\gamma = 0$. Furthermore, substituting $\sigma = \frac{3k}{8}\Theta_f^2$ in Eq. (16) and converting to original variables gives

$$\gamma^* = \pi/2, \qquad \Theta_f^* = \sqrt{\frac{3\pi J\Theta_e}{8C_a}}$$
$$\omega_e^* = \sqrt{\frac{K_{f1}}{J}}\left(1 + \frac{9\pi K_{f2} J\Theta_e}{64 K_{f1} C_a}\right) \tag{17}$$

where (Θ_f^*, γ^*) are the equilibrium states of the system at resonance. This important result relates the peak stroke amplitude Θ_f^* at resonance and the resonant frequency ω_e^* with the parameters $\{J, K_{f1}, K_{f2}, \Theta_e, C_a\}$ of the flapping dynamics equation. It is valid quantitatively if the parameters fall within the range where σ, F, B, and k are $O(1)$ and $\epsilon \ll 1$, representing a weak nonlinear oscillator. However, the qualitative relationship is applicable to a wider range of parameters.

Figure 9 compares the frequency response (Θ_f vs ω_e) curves generated by Eq. (16) with the full and simplified thorax models generated by numerical simulation for two different values of K_{f2}/K_{f1}. For weak nonlinear stiffness (K_{f2}/K_{f1}), the frequency response of the averaged system shows a good match with the simplified and full models, as shown in Fig. 9a. In the case of relatively stronger nonlinearity, the error increases, as can be seen in Fig. 9b; however, qualitatively, the response is similar. The increased nonlinearity due to a larger value of K_{f2}/K_{f1} bends the frequency response curve toward the right. Therefore, Θ_f^* occurs at a higher value of ω_e^*. This can also be seen from Eq. (17).

A. Role of Pterostigma

For a high lift requirement, α^* should be large. However, this increases C_a and consequently reduces Θ_f^*, as can be seen in Eq. (17). For a fixed value of Θ_e, Θ_f^* can be increased by increasing J. The best way to increase J is to put a mass at the wingtip. Several insect orders (*Odonata*, *Neuroptera*, *Psocoptera*, *Hemiptera*, and *Hymenoptera*) have a concentrated mass called pterostigma located precisely in this location (Fig. 8). Its function is largely unknown in general, but in dragonflies, it is believed to be used as an inertial regulator to minimize pitch vibrations during gliding flight [25]. This, however, does not explain its role in other insects that do not glide. Based on our analysis, we propose that its main function during flapping flight is to increase stroke amplitude and, thereby, improve aerodynamic performance.

B. Stability of Flapping Motion

To check the stability of the flapping motion when excited at ω_e^*, we linearize the time-averaged system given by Eq. (14) at (Θ_f^*, γ^*) as follows:

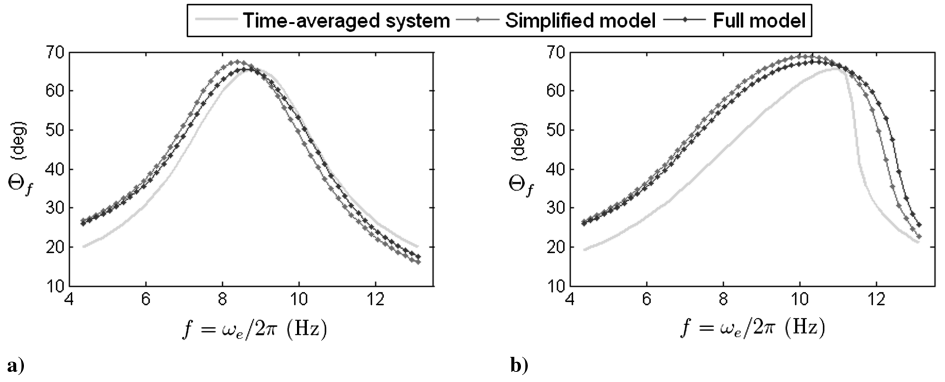

Fig. 9 Frequency response comparison of time-averaged model with simplified and full models: a) weak nonlinear stiffness $K_{f2}/K_{f1} = 0.02$ and b) strong nonlinear stiffness $K_{f2}/K_{f1} = 0.5$ shifts Θ_f^* at higher frequency. Other parameters are $F = 3.49$, $B = 3.14$, and $\epsilon = 0.1$.

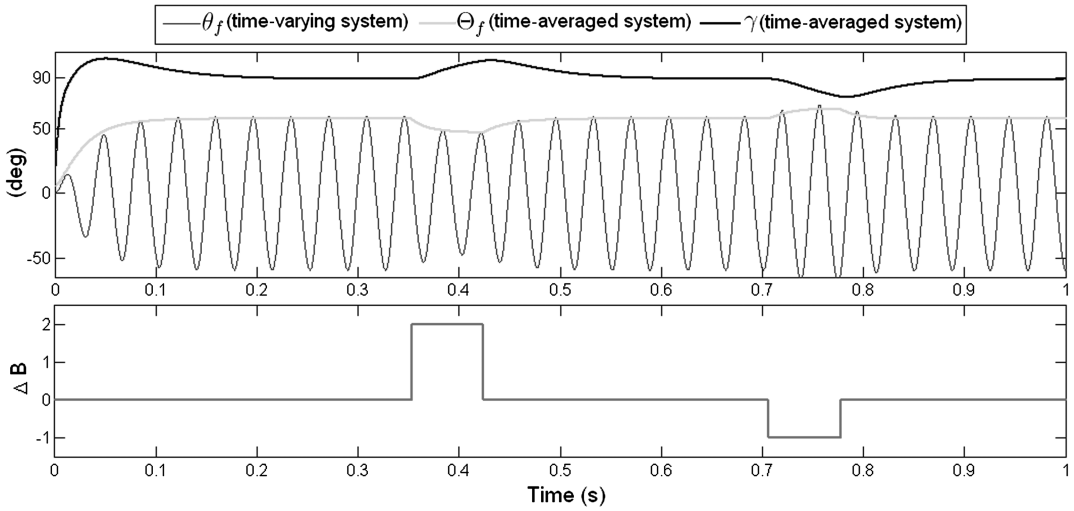

Fig. 10 Time-averaged system predicting envelope of time-varying system with error of $O(\epsilon)$. System returns to equilibrium state (Θ_f^*, γ^*) exponentially when pulse disturbance ΔB becomes zero.

$$\begin{pmatrix} \delta\dot{\Theta}_f \\ \delta\dot{\gamma} \end{pmatrix} = -\epsilon \begin{pmatrix} \sqrt{\frac{8BF}{3\pi}} & 0 \\ \frac{3K}{4}\sqrt{\frac{3\pi F}{8B}} & \frac{1}{2}\sqrt{\frac{8BF}{3\pi}} \end{pmatrix} \begin{pmatrix} \delta\Theta_f \\ \delta\gamma \end{pmatrix} \tag{18}$$

According to the theory of averaging [22,24,26], if the fixed point of the time-averaged system is exponentially stable, then the transformed time-varying system given by Eq. (11), or the original time-varying system given by Eq. (9), has a unique, exponentially stable, T-periodic orbit. Therefore, to determine the stability of the fixed point (Θ_f^*, γ^*), the eigenvalues of this system are evaluated as follows:

$$\lambda_1 = -0.4607\epsilon\sqrt{BF}, \qquad \lambda_2 = -0.9213\epsilon\sqrt{BF} \tag{19}$$

where both eigenvalues are real, distinct, and negative, which means the equilibrium point (Θ_f^*, γ^*) is exponentially stable. Therefore, the original time-varying system has an exponentially stable periodic orbit for all time. In other words, flapping motion recovers exponentially fast if disturbed. This can be seen with the help of numerical simulations in the presence of a disturbance. Figure 10 compares the numerical simulation of the time-averaged and the time-varying systems in the presence of a disturbance in damping ΔB. It can be seen that the time-averaged system very accurately predicts the envelope of the time-varying system, even during the course of the disturbance. Furthermore, as soon as the disturbance vanishes, nominal oscillations resume exponentially fast at (Θ_f^*, γ^*).

Figure 11 compares the numerical simulation of the simplified model and the full model operating at Θ_f^* in the presence of a torque disturbance τ_d, which could be due to a gust of wind. The torque disturbance τ_d can be added on the right-hand side of the flapping dynamics equation in both the simplified and the full thorax models. Figure 11 also shows this effect schematically on an insect. As the gust of wind strikes the insect from the front, it causes a torque disturbance τ_d, which shifts the mean flapping position toward the rear. After the gust ceases, normal wing motion resumes within one wing beat cycle due to exponential stability of flapping dynamics at resonance. It would be of interest to know the implications of this on insect flight dynamics.

VI. Optimal Rotational Dynamics

Once flapping dynamics, given by Eq. (4), are tuned at (Θ_f^*, ω_e^*), the rotational dynamics can be optimized to generate optimal wing rotation. For this purpose, numerical optimization was used based on the sequential quadratic programming algorithm available as the fmincon function in MATLAB. The optimization is based on a simplified thorax model given by Eqs. (4) and (5), where the flapping

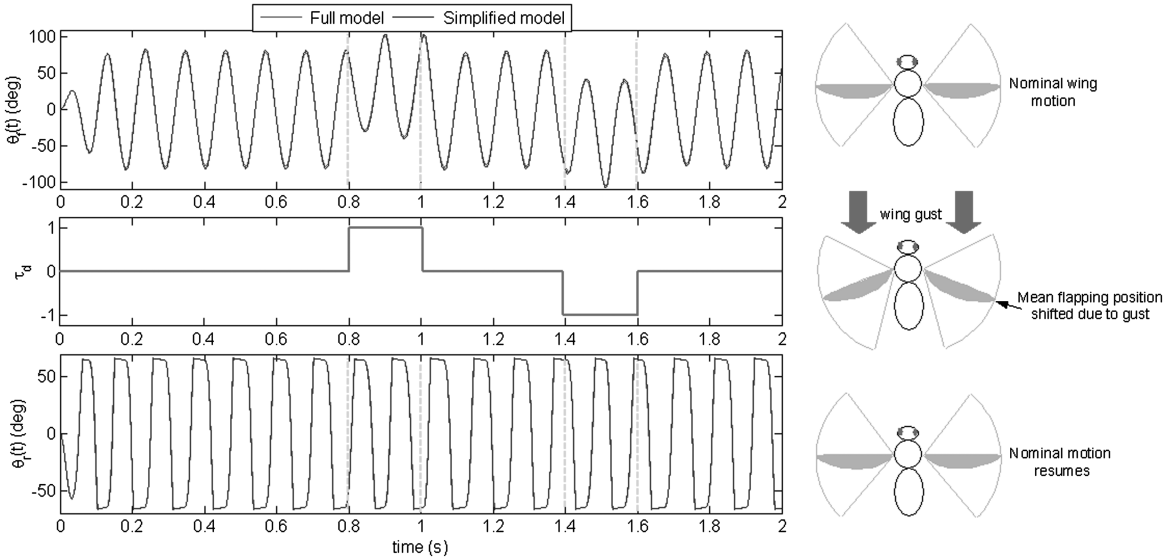

Fig. 11 Comparison of numerical simulation of full and simplified models in presence of disturbance τ_d, such as gust of wind.

Table 2 Optimization results for rotational dynamics parameters

Parameters	Initial guess	$w_3 = 0.0$	$w_3 = 0.2$
K_{r1}	1.0×10^{-5}	0.0	4.8433×10^{-4}
K_{r2}	2.0×10^{-5}	2.1177×10^{-4}	1.0×10^{-3}
δJ_y	1.0	0.5580	0.5000
δJ_{yz}	1.0	1.4145	1.1271
μ_r	1.0×10^{-9}	6.1466×10^{-9}	7.5748×10^{-9}

dynamics are already tuned at $\Theta_f^* = 90°$ and $\alpha^* = 25°$. The cost function is given by

$$f(K_{r1}, K_{r2}, \delta J_y, \delta J_{yz}, \mu_r) = w_1\left(\frac{1}{\bar{L}}\right)^2 + w_2\left(\frac{\bar{D}}{\bar{L}}\right)^2 + w_3\left(\frac{1}{T}\int_o^T |\dot{\theta}_r|\,\mathrm{d}t\right) \tag{20}$$

where w_1, w_2, and w_3 are weighting coefficients, and

$$\frac{1}{T}\int_o^T |\dot{\theta}_r|\,\mathrm{d}t$$

is the average flip speed during the wing beat cycle: in particular, during the rotation phase, since $\dot{\theta}_r \sim 0$ during the flapping phase. The cost function is designed to maximize $\bar{L}$ and $\bar{L}/\bar{D}$ as well as control ΔT through the last term. The parameters δJ_y and δJ_{yz} indicate change in J_y and J_{yz}, respectively. For instance, $\delta J_y = (J_y + \Delta J_y)/J_y$. $\delta J_y > 1$ implies increase in J_y, while a decrease gives $\delta J_y < 1$. No change means $\delta J_y = 1$. The cost function is subject to the following constraints:

$$-K_{r1} < 0, \quad -K_{r2} < 0, \quad -\mu_r < 0, \quad 0.5 - \delta J_y < 0$$
$$\delta J_y - 2 < 0, \quad 0.5 - \delta J_{yz} < 0, \quad \delta J_{yz} - 2 < 0 \tag{21}$$

where the constraints ensure that K_{r1}, K_{r2}, and μ_r remain positive and δJ_y and δJ_{yz} are bounded between 0.5 and 2. The optimization results for two values of w_3 are shown in Table 2.

The results show significant increase in rotational stiffness (K_{r1}, K_{r2}) compared with the initial values. The J_y inertia about the leading edge or rotational $\hat{y}_w$ axis is reduced, while the product inertia δJ_{yz} is increased for both values of w_3. There is also an increase in μ_r, which controls the overshoots in rotational motion (see Fig. 3).

To determine why the optimal solution improves aerodynamic performance (in particular the role played by rotational stiffness and inertia), three rotational motions were generated using 1) optimal parameters; 2) setting $K_{r1} = K_{r2} = 0$, but other parameters are optimal; and 3) $K_{r1} = K_{r2} = 0$ and original (nonoptimal) values of J_y and J_{yz}. These three kinematic patterns were generated for each value of w_3, i.e., 0 and 0.2. All six kinematic patterns were played on the robotic flapper to determine C_L and $\bar{L}/\bar{D}$. The results shown in Figs. 12e and 12f clearly show better aerodynamic performance in the optimal case. When stiffness is zero (case 2), C_L and $\bar{L}/\bar{D}$ decrease. This is because stiffness causes advanced flip compared with the other two cases, which improves aerodynamic performance (see Fig. 6).

Similarly, optimal inertia distribution also causes advanced flip compared with case 3 (nonoptimal inertia parameters). The key result is $\delta J_y \approx 0.5$, which means less mass near the trailing edge of the wing. In insect wings, the veins become thin toward the trailing edge, which minimizes J_y (Fig. 8). More interesting, the placement of pterostigma does not effect J_y, since it is located along the $\hat{y}_w$ axis near the wingtip.

The control of flip speed also shows improvement in aerodynamic performance. The case with $w_3 = 0.2$ produces slower wing rotation, which results in better aerodynamic performance compared with the faster rotation when $w_3 = 0$. The loss of lift is due to the relatively large negative lift peak generated during wing rotation when $w_3 = 0$ (see Fig. 12b). When the flip speed is minimized by letting $w_3 = 0.2$, the negative lift peak is minimized, as shown in Fig. 12d. Finally, μ_r minimizes the overshoot as the wing flips, as well as any secondary

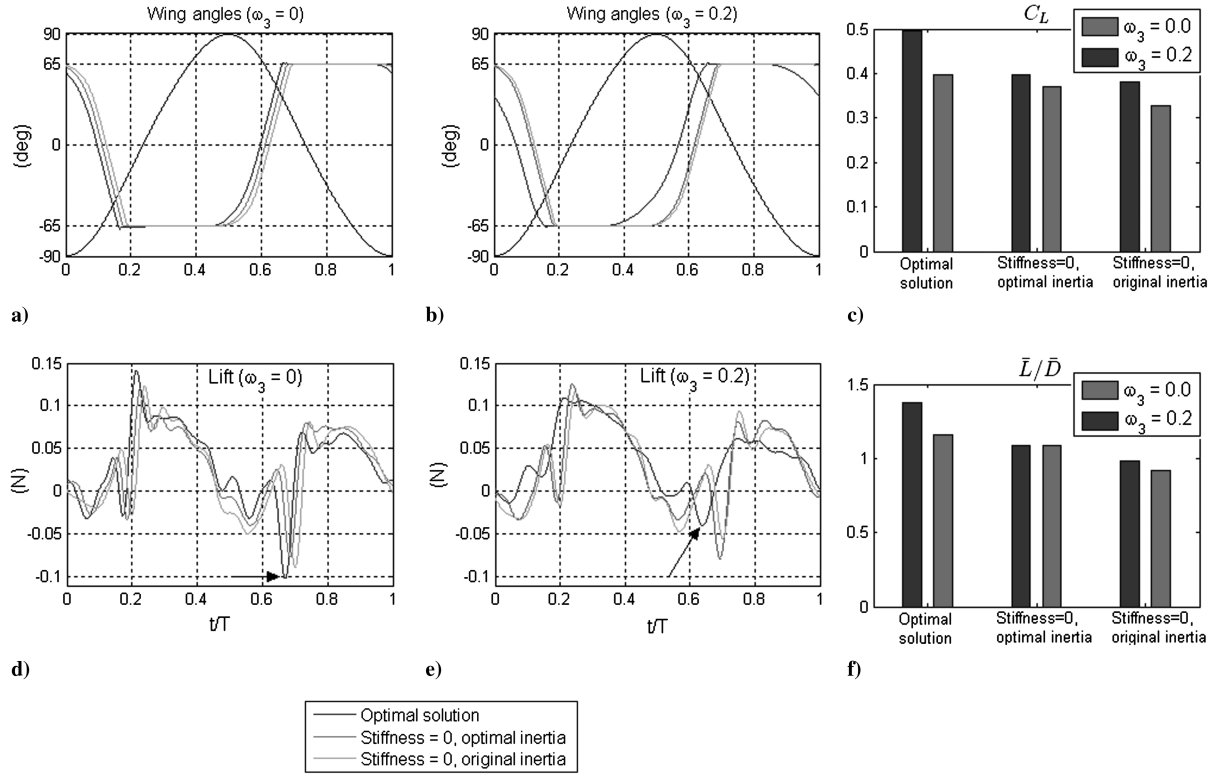

Fig. 12 Comparison of three cases of improvement of optimization of rotational dynamics C_L and $\bar{L}/\bar{D}$: kinematics generated using optimal parameters (case 1); $K_{r1} = K_{r2} = 0$, but other parameters are optimal (case 2); and $K_{r1} = K_{r2} = 0$ as well as $\delta J_y = \delta J_{yz} = 1$ (case 3). Aerodynamic data are generated by robotic flapper.

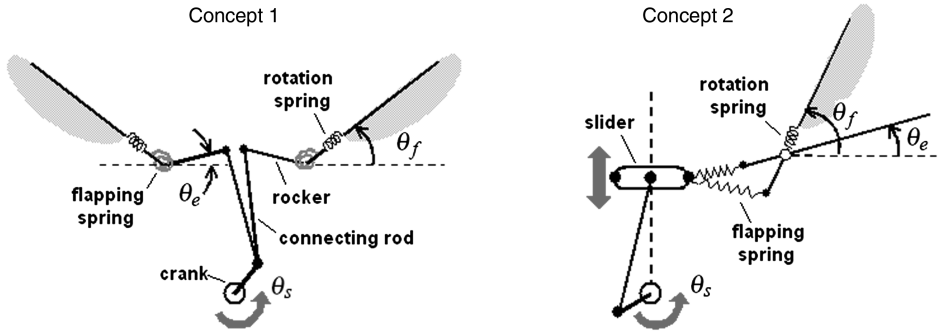

Fig. 13 Schematic showing working of two different mechanism concepts based on insect-thorax model.

oscillations in rotational motion, which are perhaps aerodynamically detrimental. Compare the nonoptimal rotational motion having overshoot and oscillations in Fig. 3 with the optimal rotational motion in Figs. 12a and 12c.

VII. Thorax-Based Design: Implementation and Testing

The goal of studying insect-thorax actuation is to develop a flapping mechanism. The model of the insect thorax can be used as a basis for the design of mechanisms that do not resemble an insect thorax but mimic its essential mechanics. Figure 13 shows schematics of two concepts. Concept 1 uses two four-bar linkages driven by a common crank to oscillate the rocker through an angle θ_e. The wing is connected to the rocker via flapping and rotation springs in series. In concept 2, a slider–crank linkage drives the wings by means of an elastic tensioner (flapping spring).

In these designs, if $\theta_e = \theta_f$, no energy storage takes place. As the crank rotates by an angle θ_s, power is transmitted to the wing through the flapping spring while rotation is generated passively, as described by the dynamics of the thorax model. This section presents the details of a prototype based on concept 1, which is also used as a testbed to investigate the significance of pterostigma and rotational stiffness.

A. Prototype Based on Concept 1

Details of a prototype mechanism are shown in Fig. 14. The crank is driven by a micro-dc motor with two-stage gear reduction. In the wing assembly, the wing base acts as a bearing for the leading edge, which can revolve freely up to $\alpha^* = 30°$ in either direction. To prevent rotation beyond α^*, a rotation lock is used (see Fig. 14c). A rod attached at the wing root and parallel to the leading edge forms the rotation spring. When the wing rotates, this rod deflects elastically and generates torsional stiffness. The entire wing assembly is mounted on top of the rocker on a common axle and connected to the rocker through elastic bands. When the wing flaps, these elastic bands are stretched and act as flapping springs (Fig. 14b).

The wing frame is made of carbon rods and covered with Japanese tissue. The pterostigma is made from a small brass tube that fits on the leading edge at the wingtip. The four-bar linkages are optimized to generate sinusoidal rocker motion at $\Theta_e = 30°$, with symmetry between the left and right sides. The mechanism weighs about 7 gf, and wing length is 10 cm.

B. Experimental Validation

The experimental setup used for mechanism characterization is shown in Fig. 15. It can measure cycle-averaged aerodynamic power $\bar{P}_a$, $\bar{L}$, Θ_f, and ω_e. $\bar{L}$ is measured by a digital weight balance with a resolution of 0.01 gf, and ω_e is measured by a stroboscope. Θ_f is measured by means of laser pointers mounted perpendicular to the stroke plane and the table. The points of light illuminate the leading edge at the extremes of the stroke and fall on the table where these are marked. The angle between the two lines originating from the marked points intersecting the flap axis is $2\Theta_f$ (Fig. 15). The flap axis

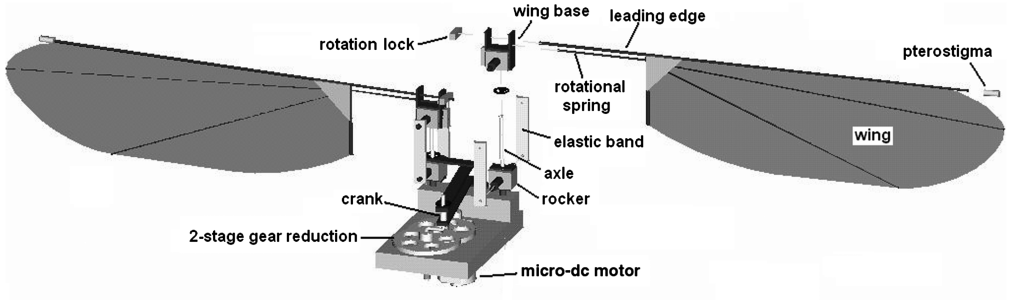

a)

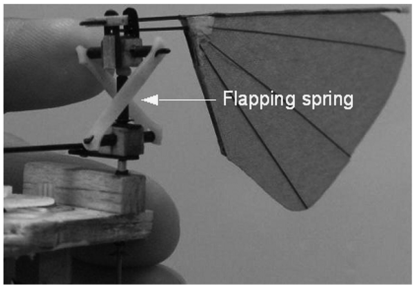

b)

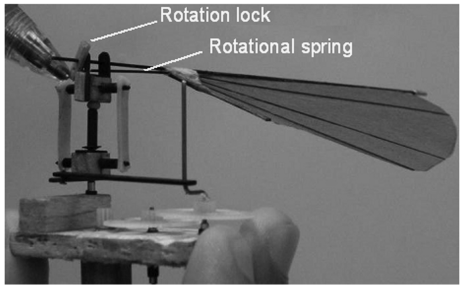

c)

Fig. 14 Details of design 1: a) CAD model showing various components, b) twist in elastic band flapping spring (actual prototype), and c) rotational spring and lock mechanism (actual prototype).

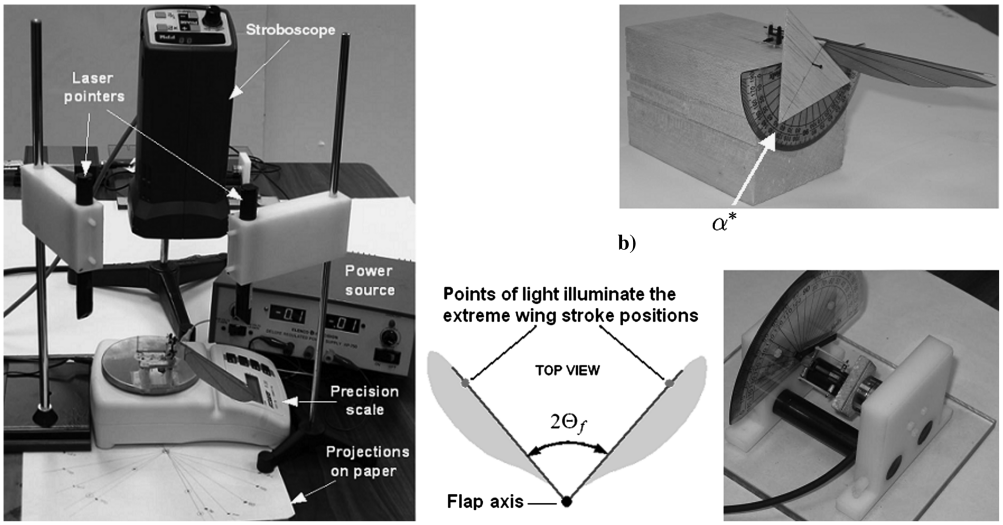

Fig. 15 Experimental setup comprising a) a stroboscope, laser pointers, and a weight balance; and b–c) custom tools for measuring α^*, spring stiffness, and motor torque constants.

is marked before the experiment using a laser pointer. This process can be repeated over a range of flapping frequencies to generate frequency response. This procedure allows fairly accurate measurements of Θ_f without expensive vision system or encoders that can affect mechanism dynamics. The cycle-averaged aerodynamic power is computed from

$$\bar{P}_a = VI - I^2 R_m - B_s \dot{\theta}_s^2 \tag{22}$$

where the voltage V and current I are supplied by a power source; R_m is the motor resistance; B_s is friction coefficient of the entire mechanism, including motor and gearbox; VI is the input power to the motor; $I^2 R_m$ is the power loss in motor windings; and $B_s \dot{\theta}_s^2$ is the friction loss. The inertia of the motor and gearbox is significant to maintain constant crank speed, i.e., $\dot{\theta}_s \sim$ constant. This means the current $I = I(\dot{\theta}_s)$ also remains constant. Therefore, $\bar{P}_a$ computed from Eq. (22) is the cycle-averaged aerodynamic power. Custom-built tools were used to measure spring stiffness and α^* (Figs. 15b and 15c), while J is computed from a detailed CAD model of the wing. At this initial phase of prototype development and performance characterization, the mechanism was tested with only one wing.

C. Results

Three cases were investigated and compared. In case A, the wing has rotational stiffness but pterostigma is not used, and in case B, pterostigma is included. In case C, pterostigma is removed, as well as rotational stiffness, by cutting the rotation spring rod. Figure 16 shows the frequency response of the three cases, along with the

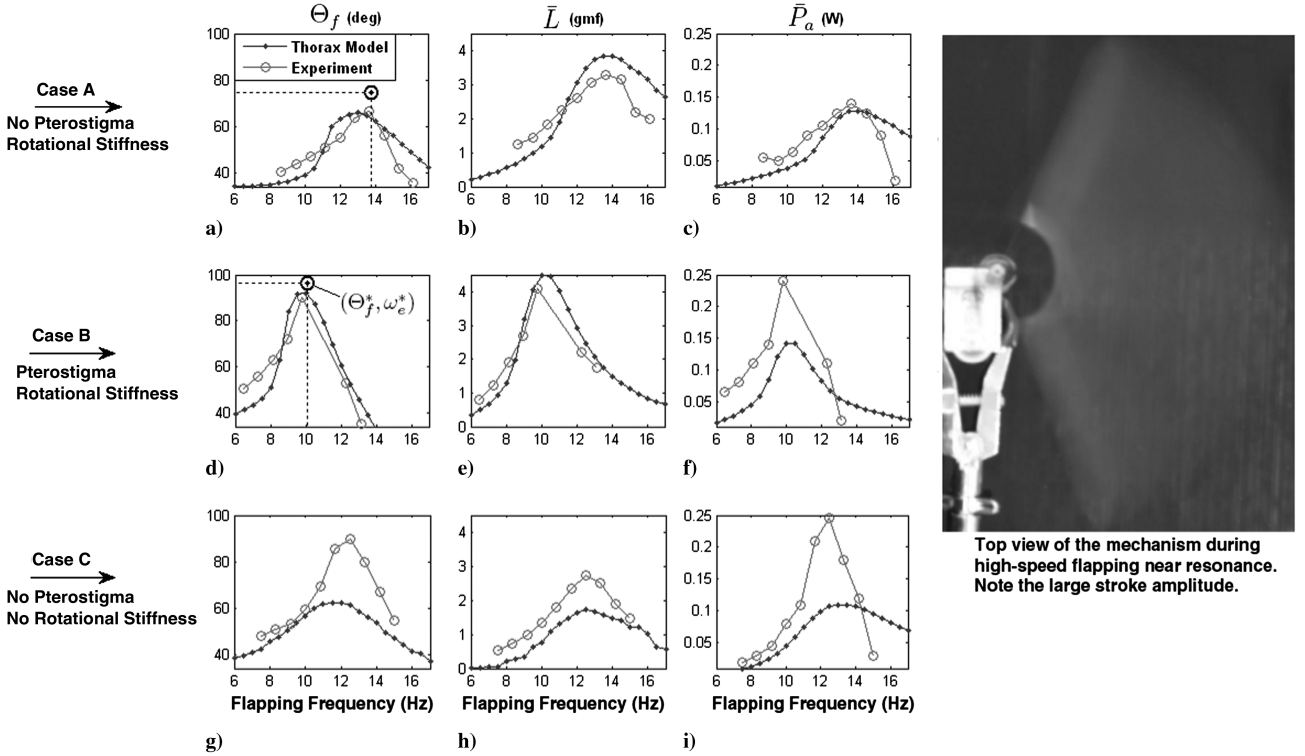

Fig. 16 Frequency response of mechanism in terms of Θ_f, $\bar{L}$, and $\bar{P}_a$ for three cases: a, b, and c. See text for details.

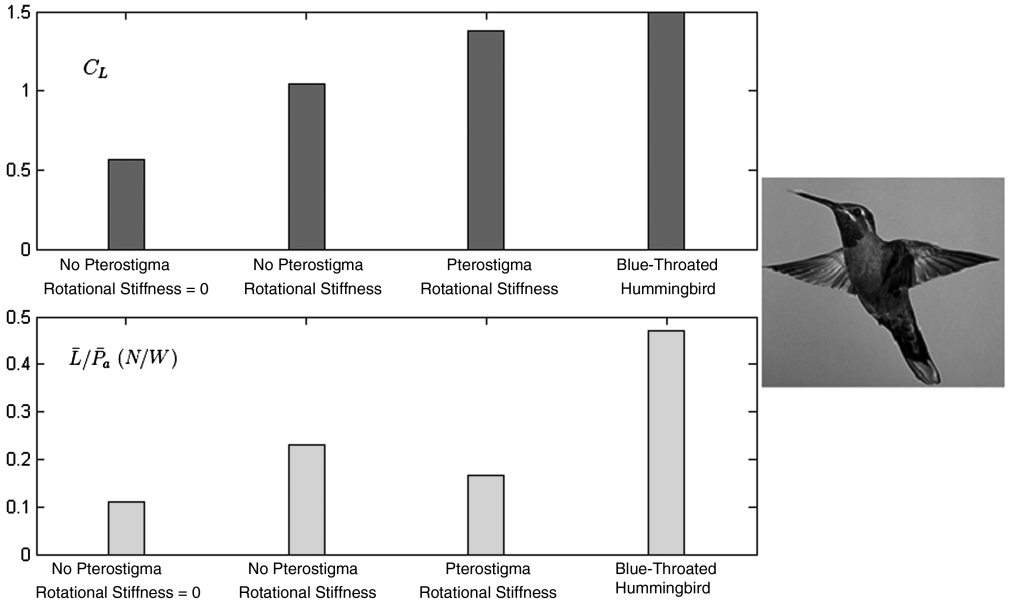

Fig. 17 Comparison of aerodynamic performance of thorax-based design with hummingbird.

frequency response generated by the full thorax model using numerical simulation.

The experimental data match very well with the full thorax model for cases A and B in terms of the shape of the curves, as well as the frequencies at which peak values of Θ_f, $\bar{L}$, and $\bar{P}_a$ occur. Figures 16a and 16d also show the point (Θ_f^*, ω_e^*) predicted by Eq. (17), which estimates ω_e^* very accurately, while Θ_f^* is overestimated due to the approximate constant damping C_a. A comparison of the plots for cases A and B show that pterostigma increases Θ_f^* and $\bar{L}$ and reduces ω_e^*. However, $\bar{P}_a$ also increases significantly compared with case A, and it is more than what the thorax model predicts, as shown in Fig. 16f.

The results of case C should be compared with case A, because the only difference is the removal of rotational stiffness in case C. The plots show that removing rotational stiffness results in significant reduction of $\bar{L}$ (compare Figs. 16b and 16e) and significant increase in $\bar{P}_a$ (compare Figs. 16c and 16f). Furthermore, Θ_f^* is much larger (compare Figs. 16a and 16g). However, even with large Θ_f^*, the aerodynamic performance is poor compared with case A. This validates the importance of rotational stiffness in flapping-wing flight.

Overall, theoretical models compare well with experimental data. The inaccuracies in Fig. 16 (see Figs. 16f–16i) are probably due to aerodynamic effects not captured by the aerodynamic model. The maximum lift generated is 4.15 gf at roughly 10 Hz (see Fig. 16e). The aerodynamic power required to generate this lift is 0.24 W (see Fig. 16f). The FWMAV will require 10–15 gf of lift per wing. Lift can be increased by increasing flapping frequency and α^*. The required aerodynamic power will also increase, but the current motor is powerful enough to cope with the increased power requirements. Furthermore, tiny brushless motors are now available, which are lighter and more powerful.

Figure 17 compares the performance of the mechanism operating at resonance with the blue-throated hummingbird, which operates at roughly the same Re number (11,000–18,000) [21]. The results show that pterostigma and rotational stiffness improve aerodynamic performance; however, a hummingbird outperforms the current thorax-based design by a large margin. The superior performance is most likely due to better aerodynamic design of hummingbird wings.

VIII. Conclusions

The flapping mechanism concept presented in this paper mimics the essential mechanics of the insect thorax and not merely the wing kinematics of a particular insect. The wing motion comes naturally from the dynamics of the system, which can be optimized for peak aerodynamic performance. To achieve this, kinematic parameters were identified that qualitatively describe the wing motion. Aerodynamic tests on a robotic flapper revealed the optimal values of these kinematic parameters in order to achieve maximum cycle-averaged lift and the lift-to-drag ratio. Nondimensional analysis of the thorax model showed that the flapping dynamics can be decoupled from the rotational dynamics. Perturbation analysis was used to tune the flapping dynamics at resonance, while numerical optimization was used to find the optimal parameters of the rotational dynamics equation.

The key findings of this analysis are the roles played by pterostigma and rotational stiffness in improving aerodynamic performance. A prototype mechanism was designed and fabricated to validate the theoretical findings. Experimental evaluation confirmed the aerodynamic importance of rotational stiffness and pterostigma in insect wings. Additionally, the thorax-based mechanism is simple and lightweight, and it shows significant lift generation capability, which can be enhanced further by the use of more powerful microbrushless motors.

Finally, the work presented in this paper also contributes to the emerging area of biologically inspired designs and provides motivation for further biological research in order to understand the importance of pterostigma and rotational stiffness in insect flight.

Acknowledgments

The authors gratefully acknowledge the funding of the National Science Foundation and the U.S. Army Research Office in support of this work.

References

[1] Ellington, C. P., "The Aerodynamics of Hovering Insect Flight. VI: Lift and Power Requirements," *Philosophical Transactions of the Royal Society of London Series B, Biological Sciences*, Vol. 305, No. 1122, 1984, pp. 145–181. doi:10.1098/rstb.1984.0054

[2] Dudley, R., *The Biomechanics of Insect Flight, Form, Function and Evolution*, Princeton Univ. Press, Princeton, NJ, 2000.

[3] Weis-Fogh, T., "Energetics of Hovering Flight in Hummingbirds and in *Drosophila*," *Journal of Experimental Biology*, Vol. 56, 1972, pp. 79–104.

[4] Zbikowski, R., Galinski, C., and Pedersen, C. B., "Four-Bar Linkage Mechanism for Insectlike Flapping Wings in Hover: Concept and an Outline of its Realizations," *Journal of Mechanical Design*, Vol. 127, No. 4, July 2005, pp. 817–824. doi:10.1115/1.1829091

[5] Banala, S. K., and Agrawal, S. K., "Design and Optimization of a

Mechanism for Out-of-Plane Insect Wing-Like Motion with Twist," *Journal of Mechanical Design*, Vol. 127, No. 4, July 2005, pp. 841–844. doi:10.1115/1.1924474

[6] Raney, D. L., and Slominski, E. C., "Mechanization and Control Concepts for Biologically Inspired Micro Aerial Vehicles," *AIAA Guidance, Navigation and Control Conference*, AIAA Paper 2003-5345, 2003.

[7] Tantanawat, T., and Kota, S., "Design of Compliant Mechanisms for Minimizing Input Power in Dynamic Applications," *Journal of Mechanical Design*, Vol. 129, No. 10, Oct. 2007, pp. 1064–1075. doi:10.1115/1.2756086

[8] Dickinson, M. H., Lehmann, F. O., and Sane, S. P., "Wing Rotation and the Aerodynamic Basis of Insect Flight," *Science*, Vol. 284, No. 5422, June 1999, pp. 1954–1960. doi:10.1126/science.284.5422.1954

[9] Sane, S. P., and Dickinson, M. H., "The Control of Flight Force by a Flapping Wing: Lift and Drag Production" *Journal of Experimental Biology*, Vol. 204, No. 15, May 2001, pp. 2607–2626.

[10] Altshuler, D. L., Dickson, W. B., Vance, J. T., Roberts, P. R., and Dickinson, M. H., "Short Amplitude High Frequency Wing Strokes Determine the Aerodynamics Of Honeybee Flight," *Proceedings of the National Academy of Sciences of the United States of America*, Vol. 102, No. 50, Dec. 2005, pp. 18,213–18,218. doi:10.1073/pnas.0506590102

[11] Deng, X., Schenato, L., Wu, W. C., and Sastry, S., "Flapping Flight for Biomimetic Robotic Insects: Part I System Modeling," *IEEE Transactions on Robotics*, Vol. 22, No. 4, Aug. 2006, pp. 776–788. doi:10.1109/TRO.2006.875480

[12] Avadhanula, S., Wood, R. J., Steltz, E., Yan, J., and Fearing, R. S., "Lift Force Improvements for the Micromechanical Flying Insect," *Proceedings of the IEEE/RSJ International Conference on Intelligent Robots and Systems*, Las Vegas, NV, Vol. 2, IEEE Publ., Piscataway, NJ, Oct. 2003, pp. 1350–1356.

[13] Wood, R. J., "The First Takeoff of a Biologically Inspired At-Scale Robotic Insect," *IEEE Transactions on Robotics*, Vol. 24, No. 2, April 2008, pp. 341–347. doi:10.1109/TRO.2008.916997

[14] Khan, Z. A., and Agrawal, S. K., "Modeling, Optimal Kinematics and Flight Control of Bio-Inspired Flapping Wing Micro Air Vehicles," Ph.D. Thesis, Univ. of Delaware, Newark, DE, 2009.

[15] Khan, Z. A., Steelman, K., and Agrawal, S. K., "Development of Insect Thorax Based Flapping Mechanism," *IEEE International Conference on Robotics and Automation*, Kobe, Japan, IEEE Publ., Piscataway, NJ, 2009, pp. 3651–3656. doi:10.1109/ROBOT.2009.5152822

[16] Wootton, R. J., "Functional Morphology of Insect Wings," *Annual Review of Entomology*, Vol. 37, 1992, pp. 113–140. doi:10.1146/annurev.en.37.010192.000553

[17] Usherwood, J. R., and Ellington, C. P., "The Aerodynamics of Revolving Wings. I," *Journal of Experimental Biology*, Vol. 205, pp. 1547–1564, 2002.

[18] Walker, J. A., "Rotational Lift: Something Different or More of the Same?," *Journal of Experimental Biology*, Vol. 205, 2002, pp. 3783–3792.

[19] Khan, Z. A., and Agrawal, S. K., "Wing Force and Moment Characterization of Flapping Wings for Micro Air Vehicle Application," *Proceedings of the 2005 American Control Conference*, Vol. 3, IEEE Publ., Piscataway, NJ, 2005, pp. 1515–1520. doi:10.1109/ACC.2005.1470180

[20] Ellington, C. P., "The Novel Aerodynamics of Insect Flight: Applications to Micro-Air Vehicles," *Journal of Experimental Biology*, Vol. 202, No. 23, 1999, pp. 3439–3448.

[21] Chai, P., and Millard, D., "Flight and Size Constraints: Hovering Performance of Large Hummingbirds Under Maximal Loading," *Journal of Experimental Biology*, Vol. 200, No. 21, 1997, pp. 2757–2763.

[22] Guckenheimer, J., and Holmes, P., *Nonlinear Oscillations, Dynamical Systems, and Bifurcations of Vector Fields*, Springer, New York, 2002.

[23] Nayfeh, A. H., *Introduction to Perturbation Techniques*, Wiley, New York, 1980.

[24] Khalil, H. K., *Nonlinear Systems*, 3rd ed., Prentice–Hall, Upper Saddle River, NJ, Dec. 2001.

[25] Norberg, R., "The Pterostigma of Insect Wings an Inertial Regulator of Wing Pitch," *Journal of Comparative Physiology*, Vol. 81, No. 1, 1972, pp. 9–22. doi:10.1007/BF00693547

[26] Sanders, J. A., and Verhulst, F., *Averaging methods in Nonlinear Dynamical Systems*, Springer–Verlag, New York, 1985.

P. Beran
Associate Editor